International Journal of Multiphase Flow 37 (2011) 732–745

Contents lists available at ScienceDirect

International Journal of Multiphase Flow

journal homepage: www.elsevier.com/locate/ijmulflow

Air–water flow properties in step cavity down a stepped chute

Stefan Felder [1], Hubert Chanson *

The University of Queensland, School Civil Engineering, Brisbane QLD 4072, Australia

ARTICLE INFO

Article history:
Received 21 December 2010
Received in revised form 24 February 2011
Accepted 27 February 2011
Available online 4 March 2011

Keywords:
Step cavity
Stepped chute
Air–water flow properties
Bubbly flow properties
Physical modelling

ABSTRACT

For the last three decades, the research into skimming flows down stepped chutes was driven by needs for better design guidelines. The skimming flow is characterised by some momentum transfer from the main stream to the recirculation zones in the shear layer developing downstream of each step edge. In the present study some physical modelling was conducted in a relatively large facility and detailed air–water flow measurements were conducted at several locations along a triangular cavity. The data implied some self-similarity of the main flow properties in the upper flow region, at step edges as well as at all locations along the step cavity. In the developing shear layer and cavity region (i.e. $y/h < 0.3$), the air–water flow properties presented some specific features highlighting the development of the mixing layer downstream of the step edge and the strong interactions between cavity recirculation and mainstream skimming flows. Both void fraction and bubble count rate data showed a local maximum in the developing shear layer, although the local maximum void fraction was always located below the local maximum bubble count rate. The velocity profiles had the same shape as the classical mono-phase flow data. The air–water flow properties highlighted some intense turbulence in the mixing layer that would be associated with large shear stresses and bubble–turbulence interactions.

1. Introduction

Stepped chutes have been used as flood release facilities of dams (Hansen and Reinhardt, 1991; Chanson, 1995; Ditchey and Campbell, 2000). The stepped design is commonly used in civil engineering for a wide range of applications and Fig. 1 illustrates a modern stepped spillway design. At large discharges, the flow skims as a coherent stream over the pseudo bottom formed by the step edges (Rajaratnam, 1990). In the step cavities, some intense and stable recirculating vortices develop through the transmission of shear stress from the main stream flow. The skimming flow is highly aerated and characterised by bubble–turbulence interactions (Chanson and Toombes, 2002) (Fig. 1B).

To date, in absence of prototype data, most physical measurements have been performed in laboratory with phase detection intrusive probes at step edges (Matos et al., 2000; Takahashi et al., 2006). There is little information on the air–water cavity flows but for the ones provided by Boes (2000), Matos et al. (2001) and Gonzalez and Chanson (2004) (Table 1). BOES (2000) and Matos et al. (2001) presented some preliminary results highlighting the strong cavity aeration. Gonzalez and Chanson (2004) showed the existence of a well-defined shear layer developing downstream of each step edge.

It is the aim of this study to expand these preliminary results and to gain a greater understanding of the cavity flows in skimming flows over a stepped chute. The study is based upon some physical modelling in a relatively large facility, and detailed air–water flow measurements were conducted at several locations along a triangular cavity (Fig. 2).

2. Experimental facility and instrumentation

The experiments were conducted in a stepped chute physical model. The chute was 1 m wide and 1 m high and equipped with a broad-crested weir followed by 10 identical steps (height: $h = 0.10$ m, length: $l = 0.20$ m). Fig. 2 illustrates the last step cavity between step edges 9 and 10.

The water discharge was deduced from total head measurements upstream of the broad-crested weir using a discharge calibration function previously obtained in situ (Gonzalez and Chanson, 2007). The air–water flow measurements were conducted with two types of needle conductivity probes. Some data were recorded with a double-tip conductivity probe with a diameter $Ø = 0.25$ mm and a longitudinal offset between sensors $\Delta x = 7.2$ mm. Another series of data was obtained with an array of two identical single-tip probes ($Ø = 0.35$ mm) separated with various transverse distances 3.3 mm $< \Delta z <$ 80.8 mm. Fig. 3 shows

* Fax: +61 7 33 65 45 99.
E-mail address: h.chanson@uq.edu.au (H. Chanson).
URL: http://www.uq.edu.au/~e2hchans/ (H. Chanson).
[1] Fax: +61 7 33 65 45 99.

0301-9322/$ - see front matter © 2011 Elsevier Ltd. All rights reserved.
doi:10.1016/j.ijmultiphaseflow.2011.02.009

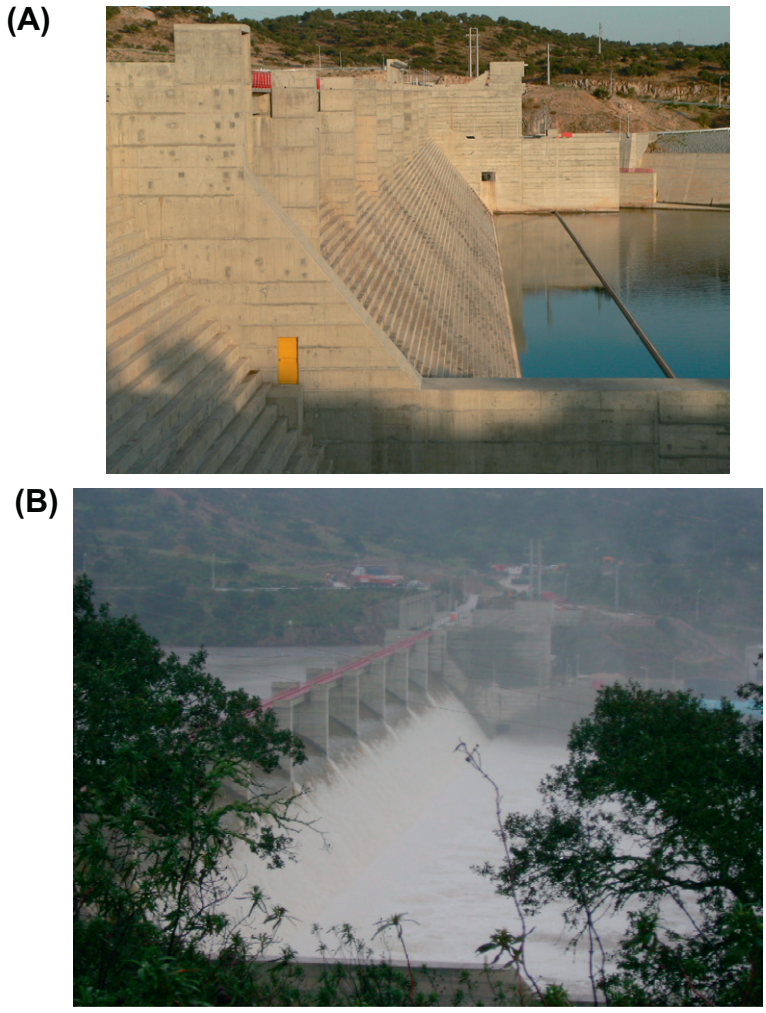

Fig. 1. Pedrogao dam stepped spillway (Portugal) – Roller compacted concrete gravity dam (H = 43 m, L = 473 m), uncontrolled overflow spillway (W = 300 m, h = 0.6 m, θ = 53.1°). (A) Stepped spillway on 4 September 2006. (B) Skimming flow on 16 January 2010 with a discharge 1000 m^3/s, Re = 1.3 × 10^7 (Courtesy of Professor Jorge MATOS).

Table 1
Experimental investigations of air–water flow properties in step cavity.

References	θ (°)	W (m)	h (m)	q_w (m^2/s)	d_c/h	Re	Measurement(s)
Boes (2000)	55	0.5	0.093	0.23	1.88	9.1 × 10^5	Void fraction
Matos et al. (2001)	21.8	1.0	0.100	0.114 and 0.182	1.1 and 1.5	4.4 and 7.2 × 10^5	Void fraction, bubble count, velocity
	30	0.4	0.025	0.026	1.62	1.2 × 10^5	Void fraction
	53.1	1.0	0.080	0.080 and 0.180	1.09 and 1.86	3.2 and 7.2 × 10^5	Void fraction
	55	0.4	0.025	0.026	1.62	1.2 × 10^5	Void fraction
Gonzalez and Chanson (2004)	15.9	1.0	0.100	0.219	1.7	8.8 × 10^5	Void fraction, bubble count, velocity
Present study	26.6	1.0	0.10	0.0147	1.33	5.9 × 10^5	Void fraction, bubble count, velocity, turbulence

Notes: d_c: critical flow depth; h: vertical step height; q_w: discharge per unit width; Re: Reynolds number defined in terms of the hydraulic diameter; W: channel width; θ: angle between slope formed by pseudo bottom and horizontal.

two probes side-by-side. The probe sensors were sampled for 45 s at 20 kHz per sensor. The displacement and the position of the probes in the direction normal to the pseudo bottom formed by the step edges were controlled by a fine adjustment system connected to a Mitutoyo™ digimatic scale unit with a vertical accuracy of less than 0.1 mm.

2.1. Experimental flow conditions

A series of observations were conducted for discharges between 0.02 and 0.237 m^3/s corresponding to Reynolds numbers between 8.2 × 10^4 and 9.4 × 10^5. A skimming flow regime was observed for discharges equal to or larger than 0.97 m^3/s and Reynolds numbers greater than 3.9 × 10^5.

A skimming flow regime with dimensionless discharge of d_c/h = 1.33 (q_w = 0.147 m^2/s) was identified as a suitable flow to provide a relatively large Reynolds number Re = 5.9 × 10^5 as well as a strong flow aeration at the measured step cavity. The air–water flow properties were measured at the downstream end of the spillway between step edges 9 and 10: i.e., 3–4 step edges downstream of the inception point of air entrainment. The measurements were conducted at the step edges and at several locations along the step

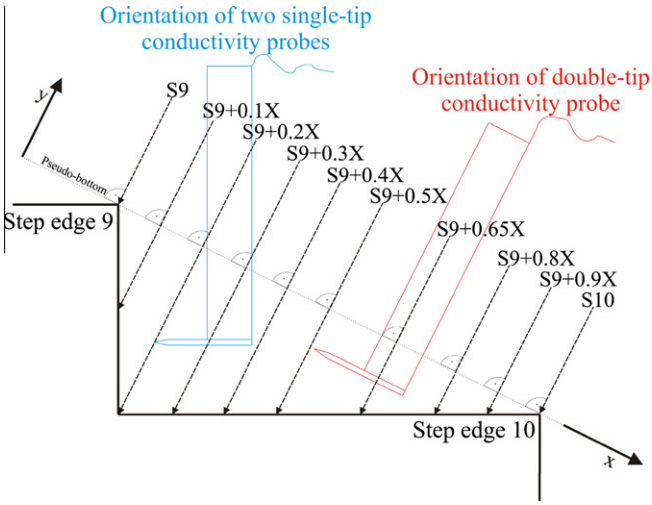

Fig. 2. Sketch of measurement locations along the step cavity and probe setup.

Fig. 3. Experimental setup with two single-tip conductivity probes side-by-side – Flow from left to right.

cavity (Fig. 2). At every location shown in Fig. 2, the measurements were conducted with both single-tip and double-tip conductivity probes. The double-tip probe was aligned with the flow direction to enable the recording of the interfacial velocities at altogether 10 measurement locations (Fig. 2). An extensive set of experiments was conducted with the array of two single-tip conductivity probe at eight streamwise locations. The probes were aligned perpendicular to the vertical step face, i.e. with an angle of 26.6° to the main flow direction. The arrangement (Figs. 2 and 3) permitted to record the air–water flow properties within the whole cavity and it was deemed appropriate since the single-tip probe output signal is little affected by the orientation of the probe with the flow (Sene, 1984; Chanson, 1988).

2.2. Signal processing

The conductivity probe signal outputs were processed using either a single threshold technique or some statistical analyses. This threshold technique was used to measure the gross parameters including the void fraction, bubble count rates and bubble chord distributions. The data accuracy on the void fraction was typically $\Delta C/C < 2\%$ for $0.03 < C < 0.95$. The smallest detectable chord length size was 0.35 mm with the single-tip probes and 0.25 mm with the double-tip probe for the experimental flow conditions and sampling rate selection (20 kHz). The accuracy on the bubble count rate was about $\Delta F/F < 5\%$.

Some additional air–water flow properties were deduced from statistical analyses of the raw signals of the conductivity probes. With the double-tip probe, these included the time-averaged interfacial velocity V and turbulent intensity Tu deduced from cross-correlation calculations. With the array of single-tip probes, the integration of the auto-correlation function R_{xx} and cross-correlation function R_{xy} from the maximum correlation $(R_{xz})_{max}$ till the first zero-crossing of the correlation curve yields the integral time scales T_{xx} and T_{xz}:

$$T_{xx} = \int_{\tau=0}^{\tau=\tau(R_{xx}=0)} R_{xx}(\tau) \times d\tau \quad (1)$$

$$T_{xz} = \int_{\tau=\tau(R_{xz}=(R_{xz})_{max})}^{\tau=\tau(R_{xz}=0)} R_{xz}(\tau) \times d\tau \quad (2)$$

where τ is the time lag. T_{xx} is the auto-correlation integral time scale which characterises the longitudinal air–water flow structure: i.e. it represents a rough measure of the longest longitudinal connection (Chanson, 2007; Chanson and Carosi, 2007). The cross-correlation integral time scale T_{xz} characterises the vortices advecting the air–water flow structure and is a function of the probe separation distance. A further air–water flow property is the advection integral length scale L_{xx} with

$$L_{xx} = V \times T_{xx} \quad (3)$$

L_{xx} is a characteristic longitudinal size of the large advecting eddies (Chanson and Carosi, 2007).

In the present study, identical experiments with identical flow conditions were repeated at identical locations with several transverse separation distances Δz, and an integral turbulent length scale was calculated:

$$L_{xz} = \int_{z=0}^{z=z((R_{xz})_{max}=0)} (R_{xz})_{max} \times dz \quad (4)$$

L_{xz} represents a characteristic dimension of the transverse turbulent integral length scale of the large vortical structures advecting the air bubbles and air–water packets. The corresponding integral time scale is:

$$T_{int} = \frac{\int_{z=0} (R_{xz})_{max} \times T_{xz} \times dz}{L_{xz}} \quad (5)$$

Lastly it is acknowledged that the recirculation motion within the step cavity might yield non-optimum conditions for bubble piercing by the probe sensor. It is not known how this would affect the probe outputs. Further the probe support might influence the main flow direction and could lead to erroneous interfacial detections. For example, for the double-tip probe, a backward directed velocity within the recirculation zone might affect the accurate cross-correlation between the two probe tips and the calculation of the interfacial velocity.

3. Basic air–water flow properties

The basic air–water flow properties were recorded at step edges for flow rates between 0.097 and 0.237 m^3/s. At each step edge, the void fraction distributions agreed very well with previous studies and showed a typical S-shape profile which agrees with the advective diffusion equation for air bubbles in turbulent flow on stepped spillways (Chanson and Toombes, 2002):

$$C = 1 - \tanh^2\left(K' - \frac{y/Y_{90}}{2 \times D_o} + \frac{(y/Y_{90} - 1/3)^3}{3 \times D_o}\right) \quad (6)$$

where C is the void fraction, y is the distance perpendicular to the pseudo bottom and Y_{90} is the distance where $C = 0.90$, K' is an integration constant and D_o is a function of the depth-averaged void fraction C_{mean} only:

$$K' = K^* + \frac{1}{2 \times D_o} - \frac{8}{81 \times D_o} \quad (7)$$

$$K^* = \tanh^{-1}(\sqrt{0.1}) = 0.32745015 \quad (8)$$

$$C_{mean} = 0.7622 \times (1.0434 - \exp(-3.614 \times D_o)) \quad (9)$$

In Fig. 4, some typical void fraction distributions are presented for all step edges downstream of the inception point of air entrainment for a discharge as a function of y/Y_{90}. The agreement with Eq. (6) is shown for two step edges. In Fig. 4, the void fraction distribution for step edge 6, which was close to the inception point of air entrainment (step edges 6–7), lies above the air-concentration profiles for the step edges further downstream. This feature highlights the rapid flow aeration downstream of the inception point of aeration and seems to be characteristic for skimming flows. It was observed for all experiments in the present study.

Some typical dimensionless bubble count rate distributions $F \times d_c/V_c$ are illustrated in Fig. 5 for skimming flows as a function of y/Y_{90}, where F is the bubble count rate defined as the number of water-to-air interfaces detected per second. The terms of the dimensionless bubble count rate $F \times d_c/V_c$ include the critical flow depth $d_c = \sqrt[3]{q_w^2/g}$ and the critical flow velocity $V_c = \sqrt{g \times d_c}$ respectively with q_w the discharge per unit width in m^2/s and g the gravity acceleration. The results indicated a maximum bubble count rate in the intermediate flow region for void fractions between 35% and 65% (Fig. 5). Further the data showed an increasing number of entrained air bubbles with increasing distance from the inception point of air entrainment (Fig. 5). The observations were consistent with previous studies on moderate stepped spillways with slopes ranging from 3.4° to 30° (Chanson and Toombes, 2002; Toombes, 2002; Kokpinar, 2004; Gonzalez, 2005; Carosi and Chanson, 2008; Felder and Chanson, 2009; Bung, 2009).

The relationship between void fraction and dimensionless bubble frequency presented some self-similarity:

$$\frac{F}{F_{max}} = 4 \times C \times (1 - C) \quad (10)$$

where F_{max} is the maximum bubble count rate in a cross-section. Eq. (10) is compared with experimental results in Fig. 5B. While Toombes and Chanson (2008) developed a more advanced conceptual model of the longitudinal distribution of air and water chords which yielded a closer agreement with experimental data, Eq. (10) is simple and fits reasonably well the data (Toombes, 2002; Chanson and Toombes, 2002) (Fig. 5B).

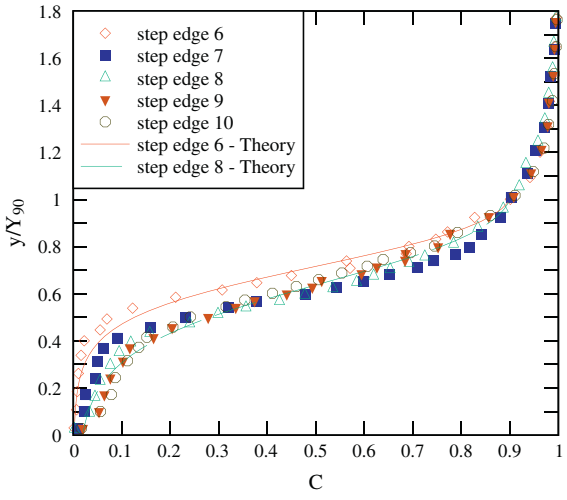

Fig. 4. Void fraction distributions in skimming flows: $d_c/h = 1.15$, $Re = 4.7 \times 10^5$, $q_w = 0.119\ m^2/s$, $h = 0.1$ m, $\theta = 26.6°$ – comparison with theory (Eq. (6)).

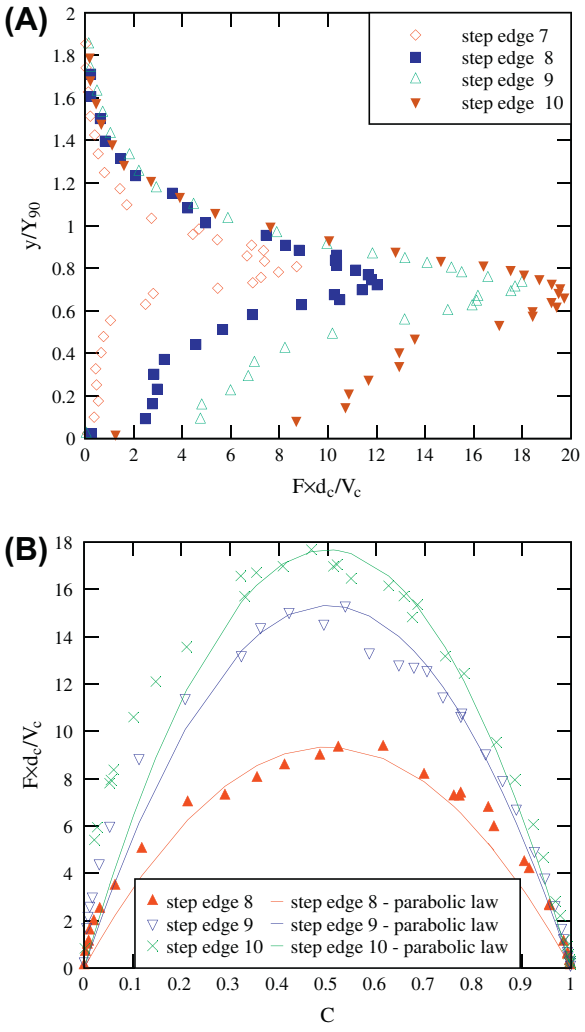

Fig. 5. Bubble count rate distributions for skimming flows. (A) Normal distributions of bubble count rate – $d_c/h = 1.45$; $Re = 6.6 \times 10^5$; $q_w = 0.167\ m^2/s$; $h = 0.1$ m; $\theta = 26.6°$. (B) Self-similar relationship between void fraction and dimensionless bubble count rate – $d_c/h = 1.57$; $Re = 7.4 \times 10^5$; $q_w = 0.187\ m^2/s$; $h = 0.1$ m; $\theta = 26.6°$ – comparison with parabolic law (Eq. (10))

Fig. 6 shows some typical normalised chord size distributions of bubble and droplet chords in the bubbly flow region ($C < 0.3$, Fig. 6A) and in the spray region ($C > 0.7$, Fig. 6B). The histograms present the chord size distributions in 0.5 mm intervals for the same discharge and at the same step edge. The distributions in both bubbly and spray flow regions showed a wide range of bubble/droplet chord sizes at each location. The spectrum of both bubble and droplet chord sizes ranged from less than 0.3 mm to more than 20 mm. Both the bubble and the droplet chord size distributions were skewed with a preponderance of small bubbles/droplets. The probability distribution of bubble chord sizes tended to follow a log-normal distribution with a mode between 0.5 and 3.0 mm (Fig. 6A). The droplet chord size probability distribution functions in the spray region were flatter and broader than those of the bubble chords, and tended also to follow some log-normal distribution (Fig. 6B). The trends for both flow regions were observed for all data sets in the present study and the results were consistent with results of some earlier studies (Chanson and

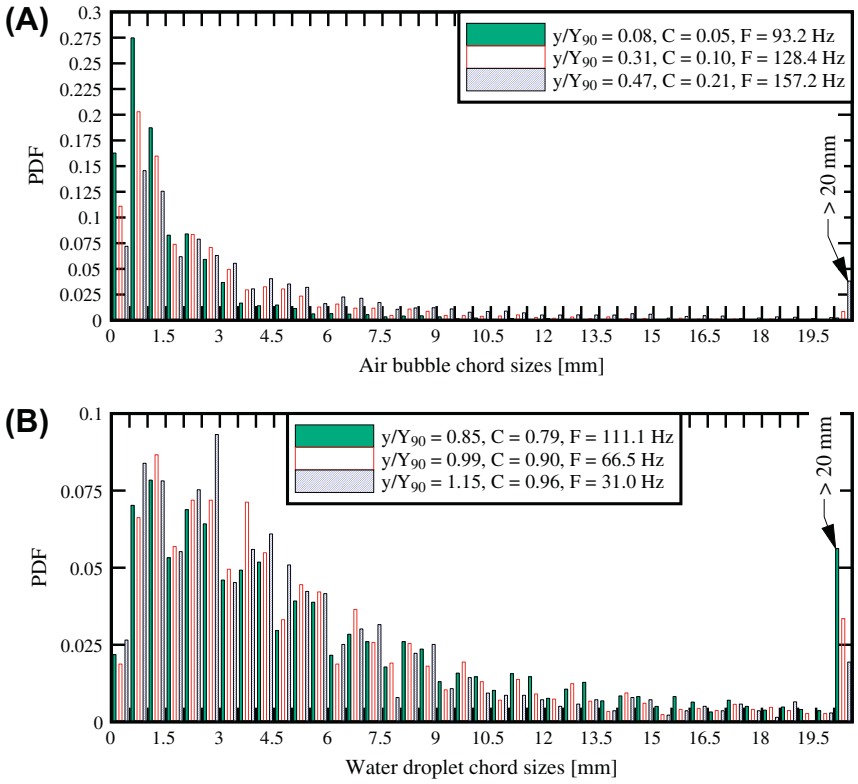

Fig. 6. Probability distribution functions of air bubble and water droplet chord sizes in skimming flows over a stepped chute – step edge 10 (four step edges downstream of the inception point of air entrainment), $d_c/h = 1.33$; $Re = 5.9 \times 10^5$; $q_w = 0.147$ m^2/s; $h = 0.1$ m; $\theta = 26.6°$.

Toombes, 2002; Takahashi et al., 2006; Chanson and Carosi, 2007; Felder and Chanson, 2009).

3.1. Interfacial velocity and turbulence intensity distributions

At all step edges downstream of the inception point of air entrainment, the distributions of time-averaged interfacial velocity are presented in Fig. 7, with the dimensionless interfacial velocity V/V_{90} distributions as a function of y/Y_{90} where V is the time-averaged velocity and V_{90} is the characteristic air–water velocity at $y = Y_{90}$. All data were correlated with a power law commonly observed in high-velocity open channel flows:

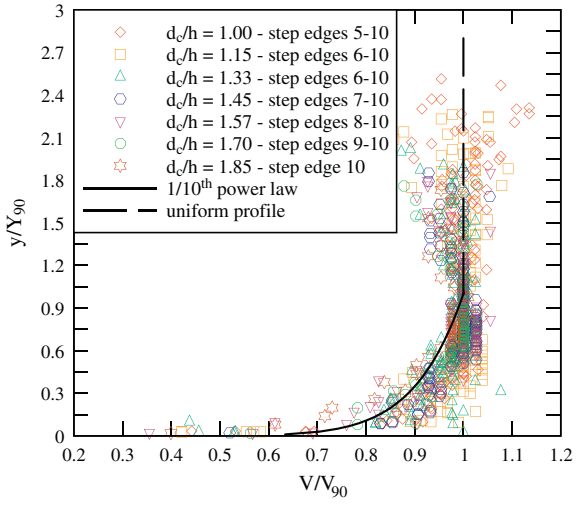

Fig. 7. Interfacial velocity distributions in skimming flows – $0.097 < Q_w < 0.237$ m^3/s, $1.0 < d_c/h < 1.85$, $h = 0.1$ m, $\theta = 26.6°$; comparison with Eqs. (11) and (12).

$$\frac{V}{V_{90}} = \left(\frac{y}{Y_{90}}\right)^{1/N} \quad 0 \leqslant y/Y_{90} \leqslant 1 \tag{11}$$

The exponent was typically $N = 10$ for skimming flows as observed previously (Chanson and Toombes, 2002; Gonzalez, 2005; Chanson and Carosi, 2007; Felder and Chanson, 2009), although some researchers found slightly different values (Boes, 2000; Bung, 2009). Further N varied from one step edge to the next one for a given flow rate (Felder and Chanson, 2009). In the upper spray region ($y/Y_{90} > 1$), a uniform velocity profile was observed:

$$\frac{V}{V_{90}} = 1 \quad 1 > y/Y_{90} \tag{12}$$

Eqs. (11) and (12) are compared with the experimental data in Fig. 7.

For all data sets, the turbulence intensity Tu was calculated based upon the shape of the cross-correlation functions between the two probe sensor signals (Chanson and Toombes, 2002). While Tu is not a true turbulence intensity u'/V as observed in mono-phase flows, it gave some valuable information about the turbulence fluctuations within the turbulent two-phase flow. Typical experimental results are presented in Fig. 8. In Fig. 8A, some typical turbulence distributions are illustrated as a function of y/Y_{90}. For all experiments in the skimming flow regime, the highest turbulence intensities were observed in the intermediate flow region for void fractions between 30% and 55%. In the bubbly flow region for $C < 30\%$, Tu had values of about 25–55% which were close to turbulence intensity observations in mono-phase flow on stepped spillways (Ohtsu and Yasuda, 1997; Amador et al., 2006). In the upper spray region ($y/Y_{90} > 1.5$), Tu tended to a value of about 20–30%. Overall the findings were consistent with previous studies of turbulence intensities on stepped spillways (Gonzalez, 2005; Chanson and Carosi, 2007; Felder and Chanson, 2009). Chanson and Toombes (2002) showed a monotonic relationship between

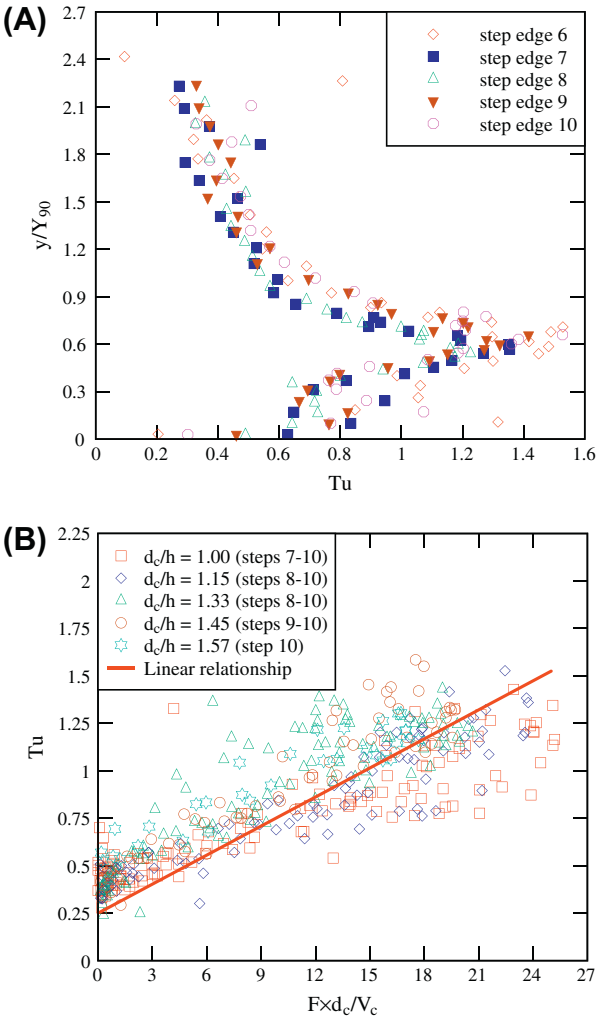

Fig. 8. Turbulence intensity distributions in skimming flows. (A) Normal distributions of turbulence intensity distributions – $d_c/h = 1.15$; $Re = 4.7 \times 10^5$; $q_w = 0.119\ m^2/s$; $h = 0.1$ m; $\theta = 26.6°$. (B) Dimensionless relationship between turbulence intensity and bubble count rate – comparison of skimming flow data ($h = 0.1$ m, $\theta = 26.6°$) at all step edges downstream of the inception point with Eq. (13).

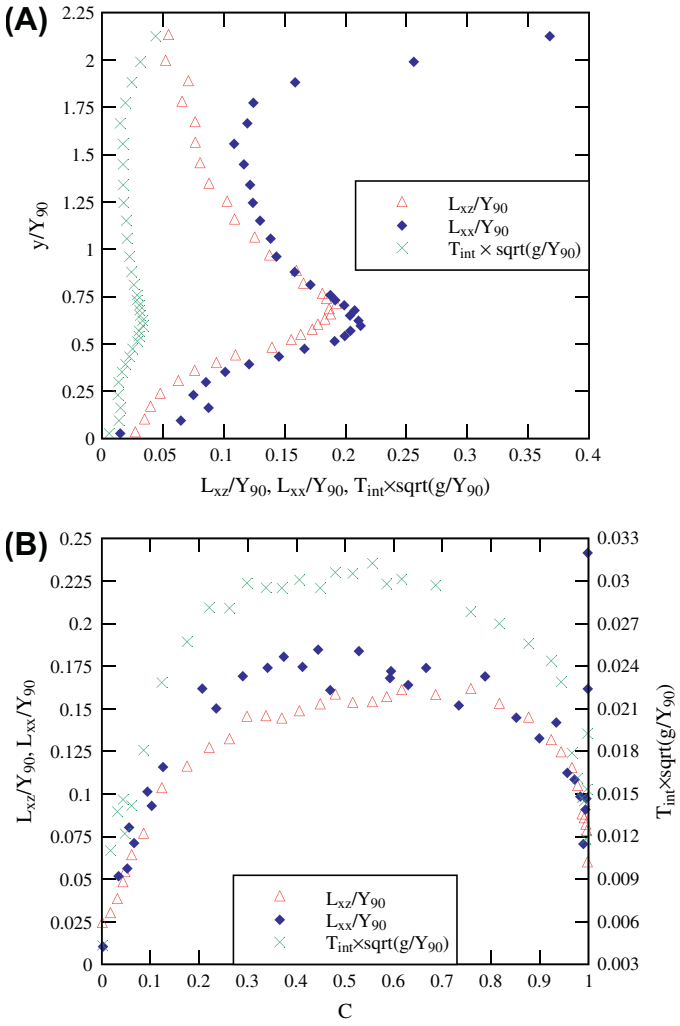

Fig. 9. Dimensionless distributions of integral turbulent time and length scales in skimming flows. (A) Dimensionless distributions as functions of y/Y_{90} for $d_c/h = 1.15$, $Re = 4.7 \times 10^5$, $q_w = 0.119\ m^2/s$, $h = 0.10$ m at step edge 10. (B) Dimensionless relationship with void fraction for $d_c/h = 1.45$, $Re = 6.6 \times 10^5$, $q_w = 0.167\ m^2/s$, $h = 0.1$ m, $\theta = 26.6°$ at step edge 10.

turbulence intensities and bubble count rates in skimming flows. Despite some scatter, the present data were best fitted by a linear correlation:

$$Tu = 0.25 + 0.051 \times \left(\frac{F \times d_c}{V_c}\right) \quad (13)$$

Fig. 8B presents a comparison between experimental data and Eq. (13). Note that the first two step edges downstream of the inception point of free-surface aeration were neither included in the finding of the linear relationship nor illustrated in Fig. 8 because the flow was rapidly-varied.

3.2. Integral turbulent time and length scales

The integral time and length scale results were integrated from the data obtained with the array of two single-tip probes with known transverse separation distance Δz. Basic results included the transverse integral turbulent time and length scales, T_{int} and L_{xz} respectively, and the advection turbulent length scale L_{xx} (Eqs. (3)–(5)). Fig. 9 illustrates some typical integral turbulent time and length scale distributions in skimming flows. The data are presented as functions of y/Y_{90} (Fig. 9A) as well as of the void fraction (Fig. 9B). The results were consistent with some features that were reported in previous studies of integral turbulent scales on stepped spillways (Chanson and Carosi, 2007; Felder and Chanson, 2009). For $0 < C < 0.95$, the distributions of integral time scales L_{xx} and L_{xz} collapsed well together, although they differed for larger void fractions in the upper spray region. The advection integral turbulent scale L_{xx} was consistently larger then the transverse length scale (Fig. 9). The integral turbulent time scale data showed some self-similarity (Fig. 9B). All integral turbulent scales exhibited a maximum value in the intermediate flow region for void fractions between 50% and 70%. In the bubbly flow region, the turbulent scales tended to zero in clear water flow ($C = 0$).

4. Air–water flow properties in step cavity

4.1. Presentation

On a stepped chute, some strong cavity recirculation is observed. The recirculations are driven by momentum transfer from the main stream flow (Chanson, 2001). Behind each step, a shear layer develops and small scale vortices are generated due

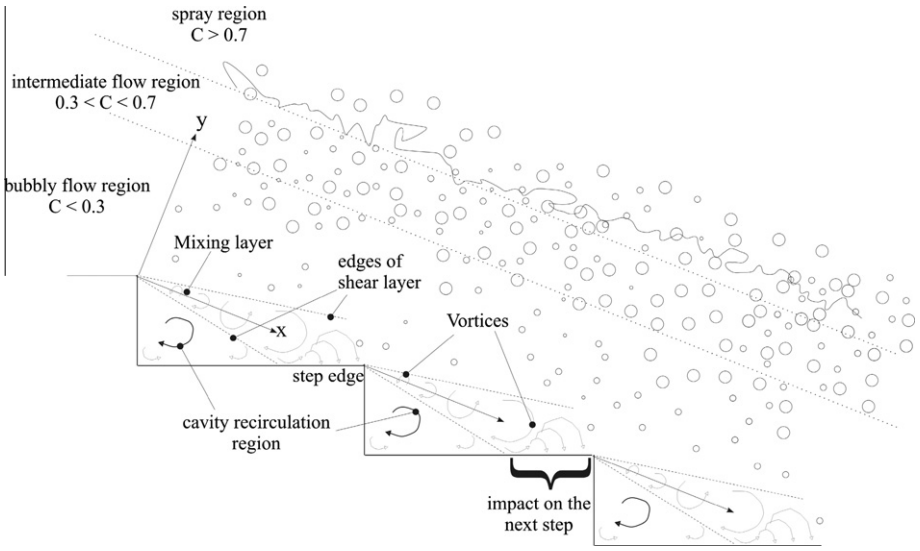

Fig. 10. Sketch of developing shear layer in skimming flows.

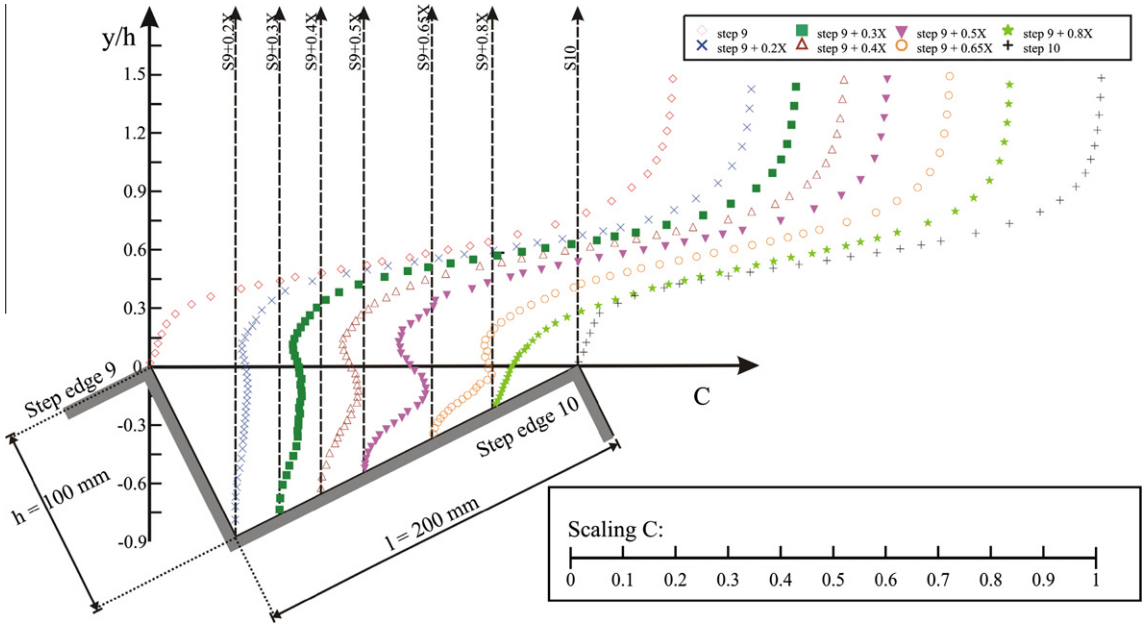

Fig. 11. Void fraction distributions along the step cavity – $d_c/h = 1.33$, $Re = 5.9 \times 10^5$, $q_w = 0.147$ m^2/s, $h = 0.1$ m, $\theta = 26.6°$.

to the form losses because of a large gradient of vorticity at the corner (Gonzalez and Chanson, 2004; Chanson and Carosi, 2007). The vortices travel downstream, combined and eventually impact on the next step edge (Fig. 10). The recirculation motion within the step cavities is three dimensional (Matos et al., 2000; Matos, 2001; Gonzalez and Chanson, 2008). Some random cavity ejections between the step cavity and the main stream skimming flows might contribute to the flow process (Chanson et al., 2002; Amador et al., 2006; Felder and Chanson, 2009). The flow processes in the step cavities are still not understood despite some first experimental studies of macroscopic air–water flow properties (Boes, 2000; Matos et al., 2001; Chanson and Toombes, 2002; Gonzalez and Chanson, 2004,2008).

The visual observations of the cavity recirculation are difficult in air–water skimming flows. A few physical studies of clear-water flows past large roughness elements and cavities add some insightful details. Some studies provided information about the generation and pairing in the three dimensional flow behind cavities (Lin and Rockwell, 2001; D'yachenko et al., 2008; Ozalp et al., 2010). Other studies detailed the momentum exchange and cavity ejection processes (Djenidi et al., 1994, 1999; Tantirige et al., 1994). The present study investigated the air–water cavity recirculation in a typical skimming flow at one cavity (Fig. 2) to provide some new insights in the sub-millimetric air–water flow properties.

4.2. Basic air–water flow properties

The void fraction distributions along the step cavity are illustrated in Fig. 11 as a function of dimensionless height perpendicular to the pseudo bottom y/h. Fig. 11 presents some distributions of void fraction at several longitudinal distance X where X is the dimensionless distance along the cavity ($0 < X < 1$) between step edges 9 and 10 (Fig. 2). The scaling for the void fraction is shown

in the figure. For the flow regions, above the pseudo bottom, all distributions were in good agreement and fitted well the typical S-shape profile which was reported in earlier studies for locations at and between the step edges (Fig. 4) (Matos et al., 2001; Chanson and Toombes, 2002; Gonzalez and Chanson, 2004; Bung, 2009). In the lower flow region ($y/h < 0.3$), however, some differences were seen. Within the step cavity, the observations showed a local maximum in void fraction within the turbulent shear layer next to the pseudo bottom (Fig. 11). Boes' (2000) data showed a similar trend for a step cavity on a slope of 50° but the location of the local void fraction maximum was closer to the step face. A comparison with the present results suggested that the size and shape of the cavity have a significant impact on the void fraction profiles in the cavity. For the present data, the maximum void fraction in the shear layer increased with increasing distance x_s from the first step edge to a maximum value at a dimensionless cavity length X of about 0.5–0.65. Further downstream, the maximum void fraction value within the cavity decreased (Fig. 11, Table 2).

Table 2
Characteristic air–water flow properties along the step cavity – $d_c/h = 1.33$, $Re = 5.9 \times 10^5$, $q_w = 0.147$ m^2/s, $h = 0.1$ m, $\theta = 26.6°$.

Location (step)	C_{mean} (double-tip)	C_{mean} (single-tip)	$(C_{cavity})_{mean}$ (single-tip)	$(C_{cavity})_{max}$ (single-tip)	$(F_{max})_{shear} \times d_c/V_c$ (single-tip)
Step 9	0.362	0.352	–	–	–
$9 + 0.1 \times X$	0.338	–	–	–	–
$9 + 0.2 \times X$	0.341	0.323	0.014	0.025	1.940
$9 + 0.3 \times X$	0.346	0.325	0.028	0.043	3.152
$9 + 0.4 \times X$	0.361	0.335	0.041	0.071	4.248
$9 + 0.5 \times X$	0.366	0.356	0.066	0.117	5.762
$9 + 0.65 \times X$	0.407	0.391	0.060	0.114	6.941
$9 + 0.8 \times X$	0.396	0.382	0.012	0.032	–
$9 + 0.9 \times X$	0.372	–	–	–	–
Step 10	0.340	0.326	–	–	–

Notes: C_{mean}: depth-averaged void fraction in the main flow ($0 < y < Y_{90}$); $(C_{cavity})_{mean}$: depth-averaged void fraction in the cavity flow ($y < 0$); $(C_{cavity})_{max}$: maximum void fraction in the cavity flow ($y < 0$); $(F_{cavity})_{shear}$: maximum bubble count rate in the shear layer; X: dimensionless distance along the cavity ($0 < X < 1$); –: data not available.

Table 2 lists some characteristic air–water flow properties along the step cavity. The data were calculated with the single-tip probe measurements; for the mean air concentration C_{mean}, the double-tip probe data are listed for comparison. Herein the depth-averaged void fraction C_{mean} was calculated above the pseudo bottom as

$$C_{mean} = \frac{1}{Y_{90}} \int_{y=0}^{y=Y_{90}} (1 - C) \times dy \quad (14)$$

where $y = 0$ at the pseudo bottom formed by the step edges. Some slight difference were observed between the single-tip and double-tip probe data, possibly resulting from the larger single-tip probe sensor size and different probe orientation. In Table 2, the mean void fraction $(C_{cavity})_{mean}$ between the cavity boundary and the pseudo bottom was calculated as:

$$(C_{cavity})_{mean} = \frac{1}{h^*} \int_{y=-h^*}^{y=0} C \times dy \quad (15)$$

where h^* is the distance from the cavity boundary to the pseudo bottom ($y = 0$) measured perpendicular to the pseudo bottom in each cross-section. $(C_{cavity})_{mean}$ and the maximum void fraction $(C_{cavity})_{max}$ were calculated at all locations between the step edges.

In addition, the bubble count rate data were recorded at all locations with the single-tip probe (Fig. 12). The results are presented in Fig. 13 at all longitudinal locations between step edges 9 and 10. The physical data highlighted a local maximum in bubble count rate in the developing shear layer (Fig. 12), and the characteristic maximum dimensionless bubble frequencies $(F_{max})_{shear} \times d_c/V_c$ are listed in Table 2 (last column) for the single-tip probe data. Above the pseudo bottom, all distributions of bubble count rates showed a typical profile with maximum values in the intermediate flow region for void fractions of about 50%. A second, much smaller peak in the bubble count rate distributions was visible close to the pseudo bottom within the shear layer. The largest values were observed just above the pseudo bottom in the centre of the step cavity. The observations of these maximum values were consistent with the observations of largest maximum void fraction in the middle of the step cavity.

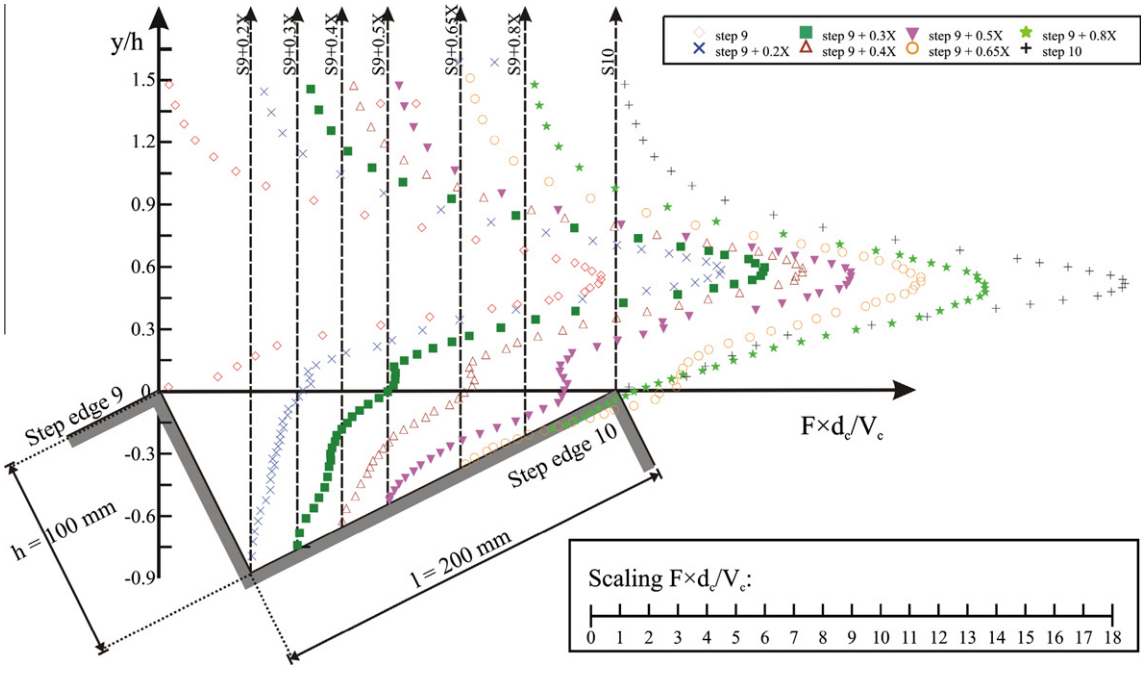

Fig. 12. Bubble frequency distributions along the step cavity – $d_c/h = 1.33$, $Re = 5.9 \times 10^5$, $q_w = 0.147$ m^2/s, $h = 0.1$ m, $\theta = 26.6°$.

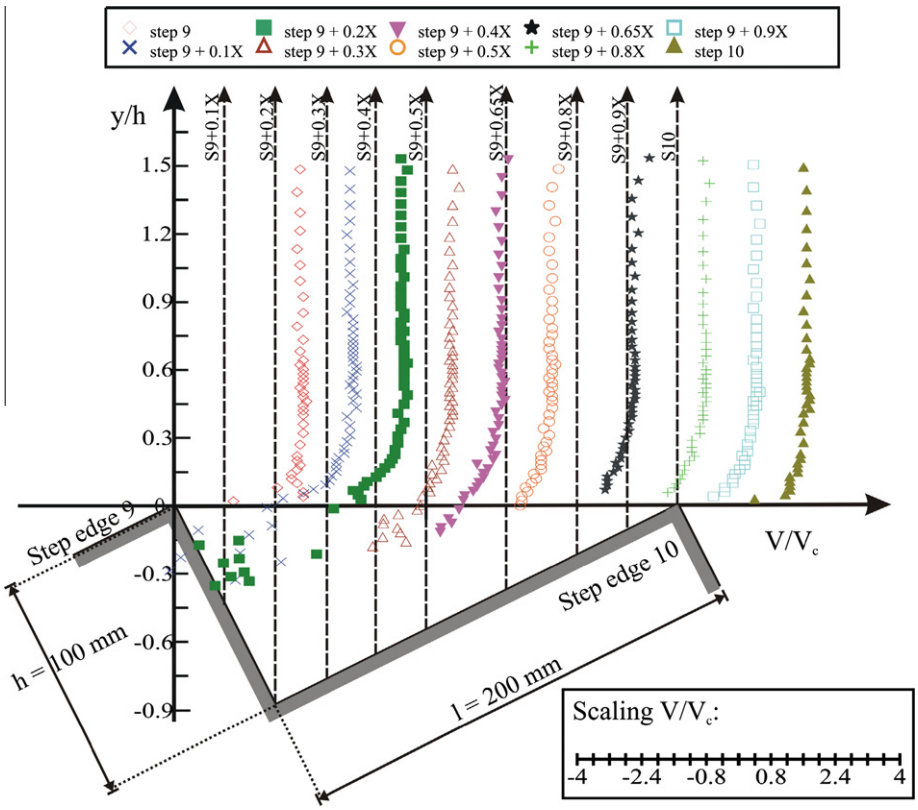

Fig. 13. Interfacial velocity distributions along the step cavity – $d_c/h = 1.33$, $Re = 5.9 \times 10^5$, $q_w = 0.147$ m^2/s, $h = 0.1$ m, $\theta = 26.6°$.

It is noteworthy that, in the shear region, the location of the local maximum in bubble count rate $(F_{max})_{shear}$ did not coincide with the location of the local maximum in void fraction $(C_{cavity})_{max}$. Rather the local void fraction maxima were located beneath the local bubble count rate maxima. The non-coincidence of $(C_{cavity})_{max}$ and $(F_{max})_{shear}$ demonstrated that the interactions between the developing shear layer and entrained air bubbles were complex. A somehow similar pattern was observed in developing shear layers of plunging jet flows and hydraulic jumps (Brattberg and Chanson, 1998; Chanson, 2010). It was suggested that the non-coincidence of air bubble diffusion layer and momentum shear layer caused the intriguing pattern, but further research is needed.

With the double-tip conductivity probe, the time-averaged interfacial velocities were recorded along the cavity and the complete results are presented in Fig. 13. All velocity distributions were similar and followed a 1/10th power law in the main flow above the pseudo bottom ($y > 0$). Along the step cavity some characteristic parameters of the velocity profiles remained almost invariant (Table 3). Beneath the pseudo bottom some negative velocities were recorded which were consistent with the visual observations of cavity recirculations. Note, however, that the double-tip probe was not designed to record negative velocities, and these recirculation data must be considered with care. Overall the findings confirmed the observations of Gonzalez and Chanson (2004) for a channel slope of 15.9°.

Table 3
Characteristic values of air–water flow properties along the step cavity – $d_c/h = 1.33$; $Re = 5.9 \times 10^5$; $q_w = 0.147$ m^2/s; $h = 0.1$ m; $\theta = 26.6°$ (double-tip probe data).

Location	U_w/V_c	V_{90}/V_c	V_0/V_c	Goertler's K	Tollmien's a'	$F_{max} \times d_c/V_c$
Step 9	2.36	3.15	2.83	–	–	17.51
9 + 0.1 × X	2.21	3.05	2.74	2.53	1.11	17.98
9 + 0.2 × X	2.26	3.10	2.79	2.60	0.34	19.12
9 + 0.3 × X	2.22	3.07	2.76	2.49	0.68	17.73
9 + 0.4 × X	2.32	3.07	2.77	3.64	0.63	17.45
9 + 0.5 × X	2.40	3.05	2.74	*8.83*	0.52	17.78
9 + 0.65 × X	2.59	3.07	2.77	*13.31*	0.47	17.99
9 + 0.8 × X	2.64	3.07	2.77	*15.89*	0.50	18.55
9 + 0.9 × X	2.57	3.15	2.83	*19.59*	0.49	19.51
Step 10	2.42	3.13	2.81	–	–	20.39

Notes: X: dimensionless distance along the cavity ($0 < X < 1$); –: data not available; Italic data: possibly incorrect data.

4.3. Self-similarity of velocity profiles in shear layer

The velocity data showed the development of a shear layer behind the upstream step edge and the data were compared with the theoretical solutions for turbulent free shear layers (Rajaratnam, 1976; Schlichting, 1979; Schetz, 1993). Tollmien (1926) developed a solution for the equations of motion in a free shear layer using Prandtl's mixing length theorem (Rajaratnam, 1976):

$$\frac{V}{V_0} = \frac{d}{d\Lambda}\left[-0.0176 \times e^{\Lambda} + 0.1337 \times e^{\Lambda/2} \times \cos\left(\frac{\sqrt{3}}{2} \times \Lambda\right) + 0.687 \times e^{\Lambda/2} \times \sin\left(\frac{\sqrt{3}}{2} \times \Lambda\right)\right] \quad (16)$$

where $\Lambda = y/(a' \times x_s)$; V_0 is the free-stream velocity, xs is the distance along a step cavity and a' is an empirical constant: $a' = (2 \times l_m^2/x_s^2)^{1/3}$ with lm the Prandl's mixing length (Gonzalez and Chanson, 2004). Goertler's (1942) solution of the equations of motion is based upon a constant eddy viscosity model (Rajaratnam, 1976):

$$\frac{V}{V_0} = \frac{1}{2} \times \left[1 + \text{erf}\left(K \times \frac{y - y_{50}}{x_s}\right)\right] \quad (17)$$

where y_{50} is the location where V/V_0 is 50%, K is a constant inversely proportional to the rate of expansion of the mixing layer, and erf is the Gaussian error function:

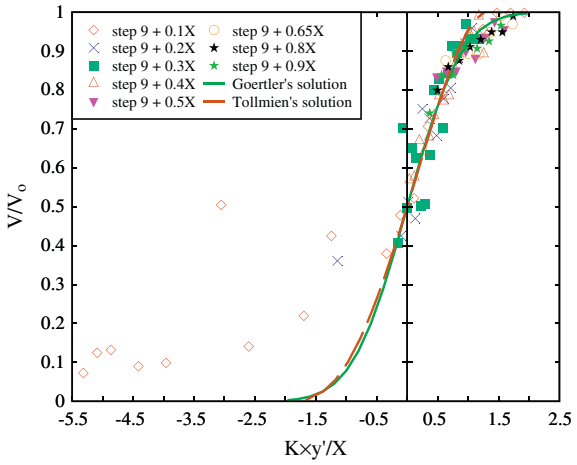

Fig. 14. Self-similarity of air–water flow velocity and comparison with theoretical solutions – $d_c/h = 1.33$, $Re = 5.9 \times 10^5$, $q_w = 0.147$ m^2/s, $h = 0.1$ m, $\theta = 26.6°$.

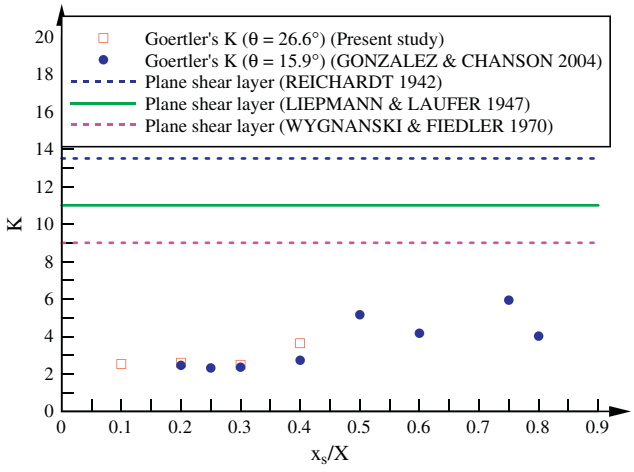

Fig. 15. Comparison between experimental results with Goerler's solution of shear layer (present study: $d_c/h = 1.33$, $Re = 5.9 \times 10^5$, $q_w = 0.147$ m^2/s, $h = 0.1$ m, $\theta = 26.6°$), air–water flow data by Gonzalez and Chanson (2004), and mono-phase flow data (Reichardt, 1942; Liepmann and Laufer, 1947; Wygnanski and Fiedler, 1970).

$$\mathrm{erf}(u) = \frac{1}{\sqrt{\pi}} \times \int_0^u e^{-t^2} \times dt \quad (18)$$

where u and t are dimensionless values to define the error function.

The interfacial velocity data are presented in a self-similar plot in Fig. 14: i.e., V/V_0 as a function of $K \times (y - y_{50})/x_s$ where the free-stream velocity V_0 was chosen to $0.9 \times V_{90}$ to be consistent with the study of Gonzalez and Chanson (2004). In Fig. 14, both Tollmien and Goertler theoretical solutions are compared with the experimental data. Overall the data agreed well with the theoretical solutions as well as with the findings of Gonzalez and Chanson (2004) with a different cavity shape. Note the discrepancy between experimental data and theory for the negative velocities which was most likely caused by the limitations of the measurement technique: the double-tip probe was not designed to record negative velocities since the probe support may interfere with the sensors.

The variable a′ in Tollmien's solution and the value K in Goertler's solution were calculated based on a best data fit and the findings are listed in Table 3 together with further characteristic flow properties. Note that the values of K might be overestimated for the measurement locations downstream of half the cavity length because it was not possible to measure the location y_{50} close to the step edge due to the design of the conductivity probe. These were highlighted in red. For plane shear layers in mono-phase flows, the values for K were deduced from studies by Reichardt (1942) (data found in Schlichting (1979)), Liepmann and Laufer (1947) and Wygnanski and Fiedler (1970). These data in terms of Goertler's K are compared in Fig. 15 with the experimental observations of two-phase flow data of the present study and of Gonzalez and Chanson (2004) for a stepped spillway with a slope of 15.9°. For both air–water flow data sets, the values of K were very close and tended to increase slightly along the step cavity towards typical values for mono-phase flow (Fig. 15). In air–water flows (Gonzalez and Chanson, 2004, present study), the values for Tollmien's a′ decreased along the step cavities (Table 3) towards typical mono-phase flow values of $a' \approx 0.09$ observed by Liepmann and Laufer (1947).

The development of the shear layer along the step cavity is shown in Fig. 16. Some characteristic values are presented: the edge of the shear layer located where $V/V_0 = 1$ and the shear layer centreline where $V/V_0 = 0.5$. The data are compared with the locations of the local maxima in void fraction and bubble count rate. The experimental results illustrate the shape of the developing

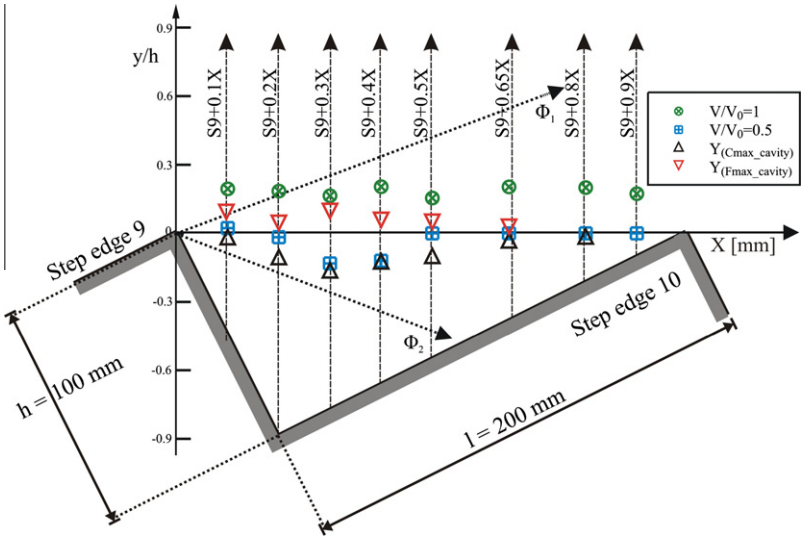

Fig. 16. Shear layer development along the step cavity – $d_c/h = 1.33$, $Re = 5.9 \times 10^5$, $q_w = 0.147$ m^2/s, $h = 0.1$ m, $\theta = 26.6°$ – location of the local void fraction and bubble count rate maxima, of the edge of the shear layer located where $V/V_0 = 1$ and of the shear layer centreline where $V/V_0 = 0.5$.

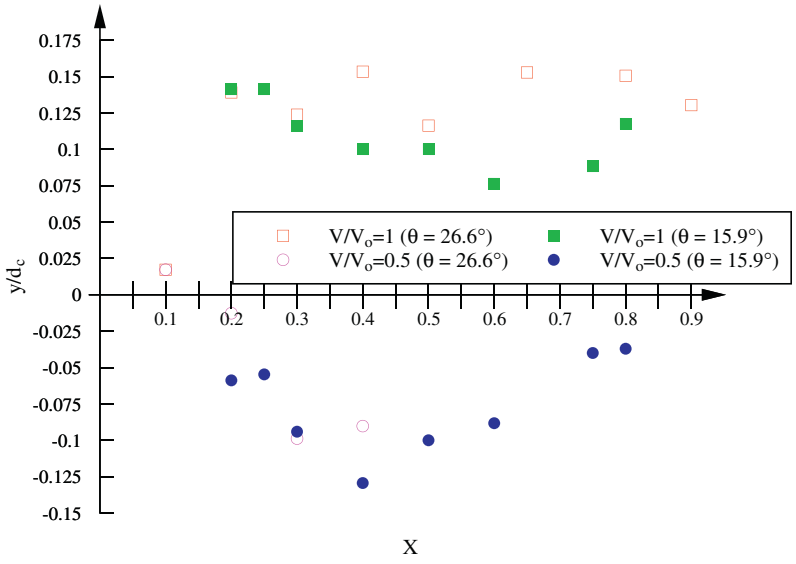

Fig. 17. Comparison of shear layer development between the present study (d_c/h = 1.33, Re = 5.9 × 10^5, q_w = 0.147 m^2/s, h = 0.1 m, θ = 26.6°) and the study of Gonzalez and Chanson (2004) (d_c/h = 1.7, Re = 8.7 × 10^5, q_w = 0.219 m^2/s, h = 0.1 m, θ = 15.9°).

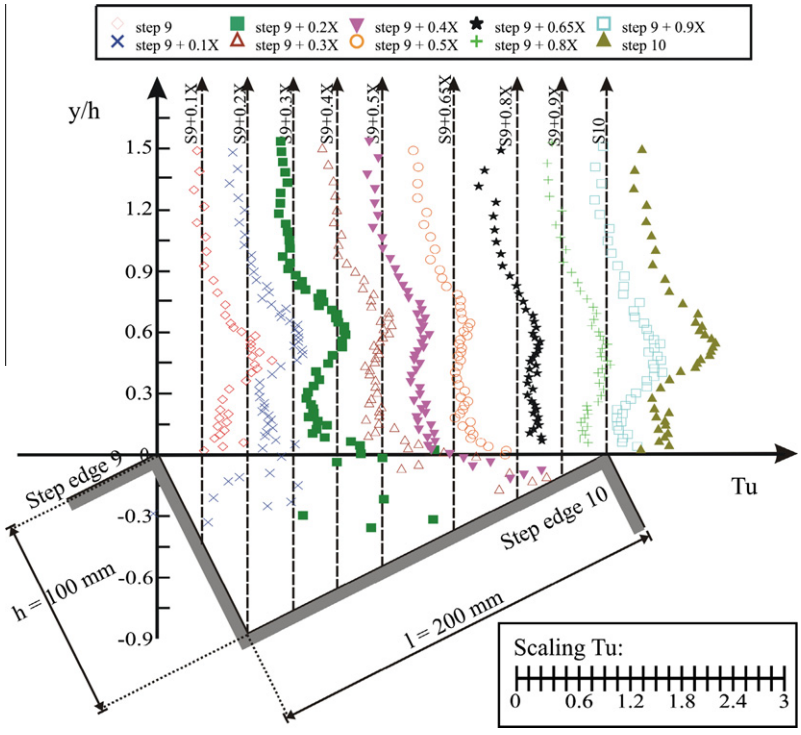

Fig. 18. Turbulence intensity distributions along the step cavity – d_c/h = 1.33, Re = 5.9 × 10^5, q_w = 0.147 m^2/s, h = 0.1 m, θ = 26.6°.

shear layer downstream of the step edge. In Fig. 16, the boundaries of the mono-phase flow shear layer are also included for the theoretical solution of Tollmien, i.e. Λ_1 = 0.981 and Λ_2 = −2.04 (Rajaratnam, 1976). The shear layer data of the present study are compared with the observations of Gonzalez and Chanson (2004) in Fig. 17 for measurement locations along the cavity. Both data sets were in agreement and highlighted the development of the shear layer in step cavities on moderate sloped stepped chutes.

4.4. Turbulent air–water flow properties

Some turbulence air–water properties were calculated at all locations along the step cavity with both double-tip and single-tip conductivity probes. The experiments with the double-tip probe yielded some information about the turbulence levels Tu. All results of the present study are presented in Fig. 18 and exhibit two distinctive features. First the turbulence levels at every location along the cavity showed large values in the intermediate flow region defined as 0.3 < C < 0.7. The finding was consistent with earlier studies at step edges (Fig. 8). Second some large turbulence levels were observed in the middle of the shear layer close to the pseudo bottom. Turbulence intensities could reach maximum levels up to 200% that were one magnitude larger than turbulence intensity observations in mono-phase flow (Wygnanski and Fiedler, 1970) and more than twice the turbulence levels in air–water flow by Gonzalez and Chanson (2004). The large turbulence

levels indicated the strong mixing in the shear layer and intense momentum exchange between cavity flow and mainstream skimming flows.

With an array of two single-tip probes, several experiments were conducted for a range of transverse separation distances $3.4 \leqslant \Delta z \leqslant 80.8$ mm, and the integral turbulent time and length scales were calculated (Eqs. (3)–(5)). The results are illustrated in Figs. 19 and 20. Fig. 19 shows the integral turbulent length and time scales, i.e. the transverse size of the large advecting vortices for the two step edges and for six locations above the step cavity. In Fig. 19A, the dimensionless integral turbulent length scales are illustrated as a function of y/h and Fig. 19B shows the corresponding dimensionless time scales. Fig. 20 shows the longitudinal development of the integral turbulent time scales along the shear layer. The data sets characterised the development of the large air–water vortical structures in the air–water flow region along a cavity and the integral turbulent scales within the recirculation zone.

For vertical locations such as $y/h > 0.3$, the distributions of integral turbulent time and length scales exhibited a similar shape for

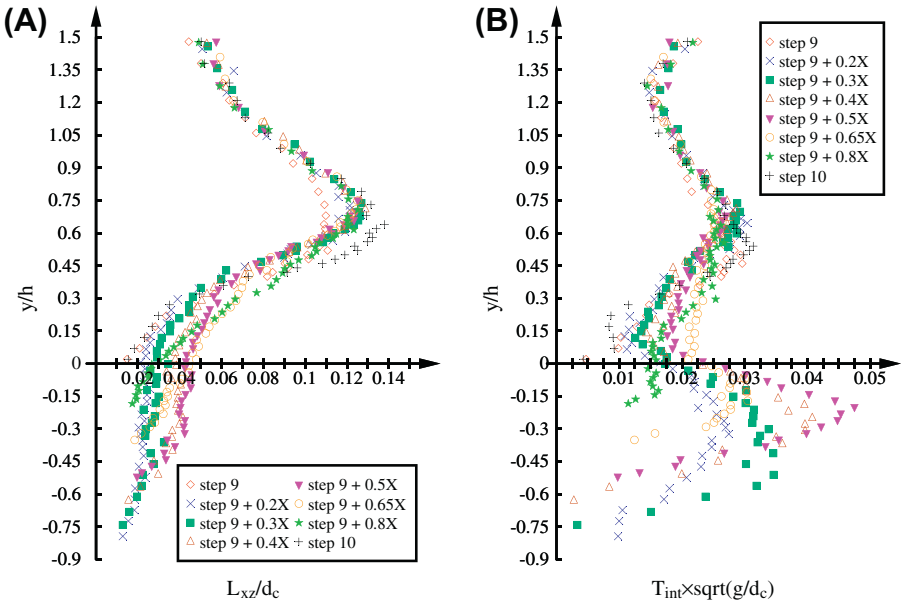

Fig. 19. Integral turbulent time and length scale distributions along the step cavity – $d_c/h = 1.33$; $Re = 5.9 \times 10^5$; $q_w = 0.147$ m^2/s; $h = 0.1$ m; $\theta = 26.6°$. (A, Left) Integral turbulent length scales. (B, Right) Integral turbulent time scales.

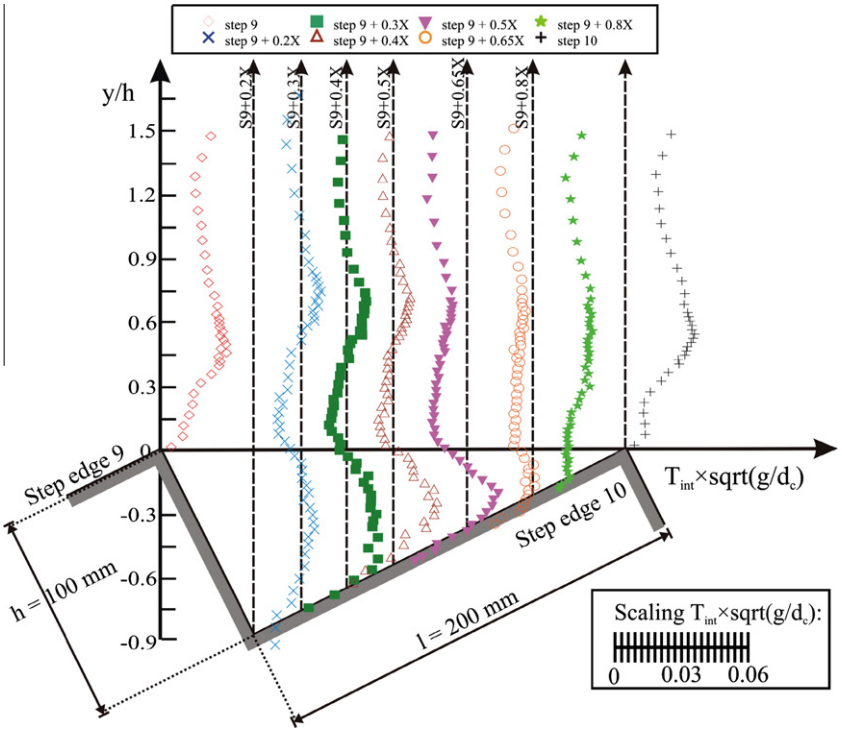

Fig. 20. Integral turbulent time scale distributions along the step cavity – $d_c/h = 1.33$, $Re = 5.9 \times 10^5$, $q_w = 0.147$ m^2/s, $h = 0.1$ m, $\theta = 26.6°$.

all locations along the step cavity suggesting some self-similarity of the large vortical structures. Maximum values were observed in the bulk of the flow $0.3 < C < 0.7$ as observed at step edges (Fig. 9). In the shear layer (i.e. $y/h < 0.3$), some differences in integral turbulent scale distributions were seen. These differences were relatively small for the integral turbulent length scales, although larger turbulent length scales were observed in the cavity beneath the pseudo bottom about the middle of the cavity. The distributions for the integral turbulent time scales showed some marked differences with larger integral turbulent time scales in the middle of the step cavity. The maximum values of these scales exceed the maximum integral turbulent time scales in the intermediate flow region (Fig. 20). Fig. 20 highlights a trend that was close to the observation of void fraction profiles along the cavity (Fig. 11), suggesting that the integral turbulent time scales distributions reflected the recirculation motion within the step cavity.

5. Conclusion

In a skimming flow above a stepped chute, both the free-stream and cavity flows are highly aerated. Some intense momentum exchange takes place in the shear layer developing downstream of each step edge. Herein some physical modelling was conducted in a relatively large facility and detailed air–water flow measurements were conducted at several locations along the triangular cavity.

For all experimental observations, the air–water flow properties showed the same trends for $y/h > 0.3$ at all locations. The finding implied some self-similarity of the main flow properties in the upper flow region, at step edges as well as at all locations along the step cavity. In the developing shear layer and cavity region (i.e. $y/h < 0.3$), the air–water flow properties presented some specific features highlighting the development of the mixing layer downstream of the step edge and the strong interactions between cavity recirculation and mainstream skimming flows.

Behind each step edge, a shear layer developed and small scale vortices travelled downstream in the region of the pseudo bottom. The present observations characterised the air–water shear layer properties. The interfacial velocity data highlighted the location of the shear layer where the momentum transfer from the mainstream flow to the cavity took place and where the recirculation motion was generated. The void fraction and bubble count rate data showed some local maxima in the developing shear layer, although the location of local maximum void fraction was always located below the local maximum bubble count rate location. A similar pattern was previously reported in developing shear layers of plunging jets and hydraulic jumps.

The void fraction distribution data presented some local maxima in void fraction in the cavity region highlighting some bubble trapping in the large scale vortices. Downstream of the cavity, the shear layer impacted on the step boundary and some ejection mechanism at the cavity downstream end transported the air bubbles out of the recirculation region. The distributions of bubble count rate highlighted some local maximum in count rate next to the pseudo bottom within the shear layer. The results implied the existence of a region of high shear stress along the cavity region, inducing some significant bubble break up linked with small scale vortices. These turbulent processes appeared to be very energetic.

Acknowledgments

The authors thank Dr. Jorge Matos (IST Lisbon) for his valuable comments. They thank further Graham Illidge, Ahmed Ibrahim, and Clive Booth (The University of Queensland) for their technical assistance. The financial support of the Australian Research Council (Grant DP0878922) is acknowledged.

References

Amador, A., Sanchez-Juny, M., Dolz, J., 2006. Characterization of the nonaerated flow region in a stepped spillway by PIV. J. Fluids Eng., ASME 128, 1266–1273.

Boes, R.M., 2000. Zweiphasenströmung und Energieumsetzung an Grosskaskaden. (Two-Phase Flow and Energy Dissipation on Cascades.) Ph.D. Thesis, VAW–ETH, Zürich, Switzerland (in German) (also Mitteilungen der Versuchsanstalt für Wasserbau, Hydrologie and Glaziologie, ETH-Zürich, Switzerland, No. 166).

Bung, D.B., 2009. Zur selbstbelüfteten Gerinneströmung auf Kaskaden mit gemäßigter Neigung. Ph.D. Thesis, Lehr-und Forschungsgebiet Wasserwirtschaft und Wasserbau, Bergische Universitaet Wuppertal, Germany (in German).

Brattberg, T., Chanson, H., 1998. Air entrapment and air bubble dispersion at two-dimensional plunging water jets. Chem. Eng. Sci. 53, 4113–4127.

Carosi, G., Chanson, H., 2008. Turbulence characteristics in skimming flows on stepped spillways. Can. J. Civ. Eng 35, 865–880.

Chanson, H., 1988. A study of Air Entrainment and Aeration Devices on a Spillway Model. Ph.D. Thesis, Department of Civil Engineering, University of Canterbury, Christchurch, New Zealand.

Chanson, H., 1995. Hydraulic Design of Stepped Cascades, Channels, Weirs and Spillways. Pergamon, Oxford, UK, p. 292 (January).

Chanson, H., 2001. The Hydraulics of Stepped Chutes and Spillways. Balkema, Lisse, The Netherlands.

Chanson, H., 2007. Bubbly flow structure in hydraulic jump. Eur. J. Mech. B/Fluids 26, 367–384.

Chanson, H., 2010. Convective transport of air bubbles in strong hydraulic jumps. Int. J. Multiphase Flow 36, 798–814. doi:10.1016/j.ijmultiphaseflow.2010.05.006.

Chanson, H., Carosi, G., 2007. Turbulent time and length scale measurements in high-velocity open channel flows. Exp. Fluids 42, 385–401.

Chanson, H., Toombes, L., 2002. Air–water flows down stepped chutes: turbulence and flow structure observations. Int. J. Multiphase Flow 28, 1737–1761.

Chanson, H., Yasuda, Y., Ohtsu, I., 2002. Flow resistance in skimming flows and its modelling. Can. J. Civ. Eng. 29, 809–819.

Ditchey, E.J., Campbell, D.B., 2000. Roller compacted concrete and stepped spillways. In: Minor, H.E., Hager (Eds.), Intl. Workshop on Hydraulics of Stepped Spillways, Zürich, Switzerland. Balkema Publ., pp. 171–178. ISBN:90 5809135X.

Djenidi, L., Anselmet, F., Antonia, R.A., 1994. LDA measurements in a turbulent boundary-layer over a D-type rough wall. Exp. Fluids 16, 323–329.

Djenidi, L., Anselmet, F., Antonia, R.A., 1999. The turbulent boundary layer over transverse square cavities. J. Fluid Mech. 395, 271–294.

D'yachenko, A.Y., Terekhov, V.I., Yarygina, N.I., 2008. Vortex formation and heat transfer in turbulent flow past a transverse cavity with inclined frontal and rear walls. Int. J. Heat Mass Transfer 51, 3275–3286.

Felder, S., Chanson, H., 2009. Turbulence, dynamic similarity and scale effects in high-velocity free-surface flows above a stepped chute. Exp. Fluids 47, 1–18.

Goertler, H., 1942. Berechnung von Aufgaben der freien Turbulenz auf Grund eines neuen Naeherungsansatzes. Calculation of the problem of free turbulence on a basis of new approximation. ZAMM 22, 244–254 (in German).

Gonzalez, C.A., 2005. An Experimental Study of Free-surface Aeration on Embankment Stepped Chutes. Ph.D. Thesis, Department of Civil Engineering, The University of Queensland, Brisbane, Australia, p. 240.

Gonzalez, C.A., Chanson, H., 2004. Interactions between cavity flow and main stream skimming flows: an experimental study. Can. J. Civ. Eng. 31, 33–44.

Gonzalez, C.A., Chanson, H., 2007. Experimental measurements of velocity and pressure distribution on a large broad-crested weir. Flow Meas. Instrum. 18, 107–113.

Gonzalez, C.A., Chanson, H., 2008. Turbulence and cavity recirculation in air–water skimming flows on a stepped spillway. J. Hydraul. Res. 46, 65–72.

Hansen, K.D., Reinhardt, K.D., 1991. Roller-compacted Concrete Dams. McGraw-Hill, New York, USA, p. 298.

Kokpinar, M.A., 2004. Flow over a stepped chute with and without macro-roughness elements. Can. J. Civ. Eng. 31, 880–891.

Liepmann, H.W., Laufer, J., 1947. Investigation of Free Turbulent Mixing. NACA Technical Note, No. 1257. National Advisory Committee for Aeronautics, Washington, DC, USA.

Lin, J.C., Rockwell, D., 2001. Organized oscillations of initially turbulent flow past a cavity. AIAA J. 39, 1139–1151.

Matos, J., 2001. Onset of skimming flow on stepped spillways. Discussion. J. Hydraul. Eng., ASCE 127, 519–521.

Matos, J., Quintela, A., Sánchez -Juny, M., Dolz, J., 2000. Air entrainment and safety against cavitation damage in stepped spillways over RCC dams. In: Minor, H.E., Hager (Eds.), Intl. Workshop on Hydraulics of Stepped Spillways, Zürich, Switzerland. Balkema Publ., pp. 69–76.

Matos, J., Yasuda, Y., Chanson, H., 2001. Interaction between free-surface aeration and cavity recirculation in skimming flows down stepped chutes. In: 29th IAHR Congress, Bejing, China, Theme D, vol. 1, pp. 611–617.

Ohtsu, I., Yasuda, Y., 1997. Characteristics of flow conditions on stepped channels. In: Proc. 27th IAHR Biennial Congress, San Francisco, USA, Theme D, pp. 583–588.

Ozalp, C., Pinarbasi, A., Sahin, B., 2010. Experimental measurement of flow past cavities of different shapes. Exp. Therm. Fluid Sci. 34, 505–515.

Rajaratnam, N., 1976. Turbulent Jets. Development in Water Science, vol. 5. Elsevier Scientific, New York, USA.

Rajaratnam, N., 1990. Skimming flow in stepped spillways. J. Hydraul. Eng., ASCE 116, 587–591.

Reichardt, H., 1942. Gesetzmaessigkeiten der freien Turbulenz (''Similarity in Free Turbulence''), vol. 414. VDI-Forschungsheft (in German).

Schetz, J.A., 1993. Boundary Layer Analysis. Prentice Hall, Englewood Cliffs, USA.

Schlichting, H., 1979. Boundary Layer Theory, seventh ed. McGraw-Hill, New York, USA, p. 817.

Sene, K.J., 1984. Aspects of Bubbly Two Phase Flow. Ph.D. Thesis, Trinity College, University of Cambridge, UK, p. 235.

Takahashi, M., Gonzalez, C.A., Chanson, H., 2006. Self-aeration and turbulence in a stepped channel: influence of cavity surface roughness. Int. J. Multiphase Flow 32, 1370–1385. doi:10.1016/j.ijmultiphaseflow.2006.07.001.

Tantirige, S.C., Iribarne, A.P., Ojha, M., Trass, O., 1994. The turbulent boundary layer over single V-shaped grooves. Int. J. Heat Mass Transfer 37, 2261–2271.

Tollmien, W., 1926. Berechnung turbulenter Ausbreitungsvorgaenge (calculation of turbulent jets). ZAMM 6, 468–478 (in German).

Toombes, L., 2002. Experimental Study of Air–Water Flow Properties on Low-gradient Stepped Cascades. Ph.D. Thesis, Dept. of Civil Engineering, University of Queensland, Australia.

Toombes, L., Chanson, H., 2008. Interfacial aeration and bubble count rate distributions in a supercritical flow past a backward-facing step. Int. J. Multiphase Flow 34, 427–436.

Wygnanski, I., Fiedler, H.E., 1970. Two-dimensional mixing region. J. Fluid Mech. 41, 327–361.